

GuideGen: A Text-Guided Framework for Full-torso Anatomy and CT Volume Generation

Linrui Dai^{1,2,*} Rongzhao Zhang^{2,*} Yongrui Yu¹ Xiaofan Zhang^{1,2,†}

¹Shanghai Jiao Tong University

²Shanghai Artificial Intelligence Laboratory

Abstract

The recently emerging conditional diffusion models seem promising for mitigating the labor and expenses in building large 3D medical imaging datasets. However, previous studies on 3D CT generation have yet to fully capitalize on semantic and textual conditions, and they have primarily focused on specific organs characterized by a local structure and fixed contrast. In this work, we present GuideGen, a controllable framework that generates anatomical masks and corresponding CT volumes for the entire torso—from chest to pelvis—based on free-form text prompts. Our approach includes three core components: a text-conditional semantic synthesizer for creating realistic full-torso anatomies; a contrast-aware autoencoder for detailed, high-fidelity feature extraction across varying contrast levels; and a latent feature generator that ensures alignment between CT images, anatomical semantics and input prompts. To train and evaluate GuideGen, we compile a multi-modality cancer imaging dataset with paired CT and clinical descriptions from 12 public TCIA datasets and one private real-world dataset. Comprehensive evaluations across generation quality, cross-modality alignment, and data usability on multi-organ and tumor segmentation tasks demonstrate GuideGen’s superiority over existing CT generation methods.

1. Introduction

The acquisition of a large quantity of medical images and their corresponding labels has always been critical for modern medical image analysis. However, due to data privacy issues and laborious annotation work, such datasets are often unavailable publicly, undermining the performance of subsequent tasks [14]. Recently trending conditional generative methods offer a promising solution to these problems: By eliminating privacy concerns and human inter-

ventions, they can generate vivid samples to an arbitrary scale, which provide significant boost to the performance of downstream applications like image segmentation and classification [25, 29, 31, 54].

Current conditional generative approaches can be categorized based on the nature of the conditions they incorporate. Semantic conditions, including organ and tumor maps, can be effectively harnessed to generate images that adhere to specific locality constraints [24, 29, 65, 66, 68]. Textual conditions like medical prompts, which are semantically rich and descriptive, can also be employed to enhance the diversity of generated images [4, 7, 9, 30, 40, 71]. However, despite their advancements, these methods fail to leverage the merits of both types of constraints, resulting in the semantic-guided models being not versatile enough to synthesize samples to a greater diversity and text-guided models not accurate enough to fully reflect exact spatial relationships among anatomical structures. Realizing this disadvantage, MedSyn [64] proposes to adopt a text-guided anatomy-aware generation pipeline that generates CT images not only conforms to anatomical masks, but also to a free-text textual guidance on a specific pulmonary disease. However, MedSyn requires paired semantics and texts as conditional input, and it only synthesizes a local region of the body (chest), which greatly limits its versatility and downstream usability. Moreover, contrary to the field of 2D medical image analysis, how to effectively incorporate textual knowledge and align it with semantic information remains largely underexplored in 3D CT synthesis [23]. This deficiency of targeted researches significantly hinders the formulation of an end-to-end, *i.e.* text to samples of masks and images, generation framework of medical CT dataset.

To overcome these limitations, we propose a novel framework GuideGen that synthesizes full-torso anatomies and CT images based on a single medical free-text input, which are constructed by incorporating patient demographic information and clinical knowledge for a potential tumor site. Naturally, GuideGen can synthesize paired samples that provides for dataset construction on down-

*Equal contribution.

†Correspondence to Xiaofan Zhang.

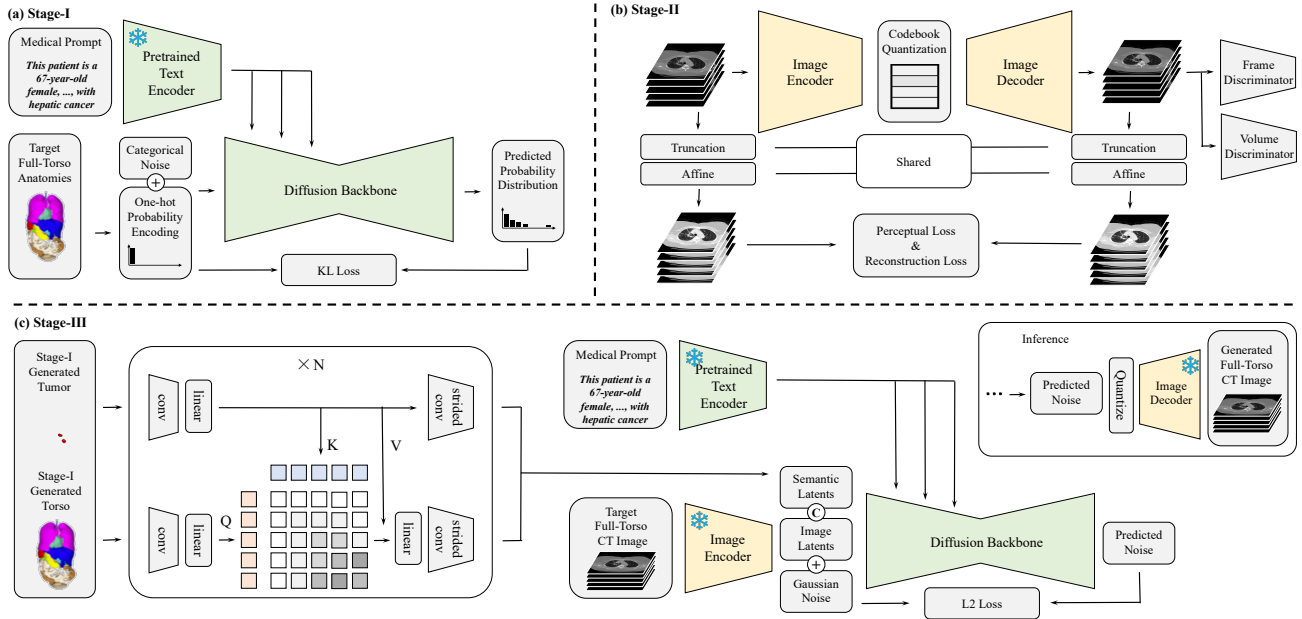


Figure 1. Overview of GuideGen. Given a medical prompt, GuideGen is able to synthesize anatomical structures that accurately reflect demographic or clinical details described in the prompt in three stages. In Stage-I, GuideGen synthesizes discrete semantic volumes that conforms to spatial features designated in the medical prompt; In Stage-II, GuideGen deploys a contrast-aware autoencoding module to accommodate large CT volumes while extracting detailed texture from all contrast levels; In Stage-III, GuideGen combines information of semantic latents derived from anatomies in Stage-I, image latents extracted in Stage-II and textual latents from the input medical prompt.

stream multi-organ and tumor segmentation tasks. It is also more user-friendly as it necessitates only an medical free-text input, empowering researchers to synthesize full-torso CT dataset with minor effort. Our GuideGen consist of three individual stages, separately for text-guided semantics synthesis, contrast-aware CT autoencoding and latent-guided CT generation. In Stage-I, we offer a text-conditional semantic synthesizer based on a categorical diffusion model to generate exact discrete label indices, unlike current practices [24] that suffer from an ambiguity problem (See Sec. 3.1). It also translates the implicit information in medical prompts onto concrete semantic conditions to better guide the subsequent CT generation. In Stage-II, we train a contrast-aware autoencoder to extract comprehensive anatomical features from multiple contrast levels, avoiding the detail degradation by truncating intensities to a specific range that favors a region of interest as per many current practices [8, 68]. In Stage-III, we utilize a diffusion latent generator that operates on the combined information of semantic latents derived from anatomies in Stage-I, image latents extracted in Stage-II and textual latents capturing demographic or clinical features in the input medical prompt.

We train and validate GuideGen on an assembly of 12 public tumor datasets and one in-house colorectal cancer dataset, which contain the multi-modal information of CT

images and medical descriptions. To testify GuideGen’s downstream usability, we further include 2 multi-organ segmentation datasets and 3 tumor segmentation datasets. Our framework achieves state-of-the-art results in sample quality, conditional consistency as well as downstream usability on segmentation tasks across multiple datasets.

Our contributions can be concluded as follows:

- We propose GuideGen, a viable and novel solution capable of performing text-based full-torso anatomy and CT generation.
- We introduce a text-conditional semantic synthesizer that avoids ambiguity in current 3D anatomy generations, a contrast-aware module to accommodate high intensity variations in full-torso CT volumes and a latent-guidance module to better preserve detailed semantic guidance.
- We conduct thorough experiments comparing the samples generated by GuideGen with 6 state-of-the-art generative frameworks from their quality, conditional consistency and downstream usability, on all of which GuideGen achieves better performances.

2. Related Works

Generative frameworks such as Energy-Based Models [17, 21], Generative Adversarial Networks [15, 61, 73], Normalizing Flows [22, 36], Variational Autoencoders [41], and Diffusion Models [32, 33, 67] encouraged myriad re-

searches on image generation due to their high authenticity and variability. Among these studies, the most advanced feature that has emerged is arguably the capacity to steer the generation process via user-defined conditions [56]. This capability allows for a high degree of precision and customization in creating images, responding directly to the specific requirements set by the user, while providing a way for the generated images to be used for dataset augmentation purposes [19, 35]. In this work, we extend the ability of current diffusion models for a text-guided anatomy and CT synthesis, which mitigates data scarcity often experienced in the field of medical image analysis.

Medical CT Synthesis on which previous endeavors undoubtedly provide some performance boost on their tasks of choice [13, 25, 29, 39, 45]. Despite their pioneering efforts, their work is confined to specific organs, which renders repeatedly retraining the network a necessity for each specific organ of interest. A lack of external guidance also underscores the need for a more flexible approach that conforms to not only descriptive texts but also to detailed semantics. Although recent work has begun to focus on these problems [40, 64], their generation processes require paired semantic and textual input to generate regional patches, which limits its downstream applicability. While a step forward, this indicates room for further development to achieve a more automated and generalized solution. This paper intends to provide a text-guided full-torso generative framework that aids to a wide range of downstream tasks.

3. Method

As illustrated in Fig. 1, GuideGen differs from current text-conditional medical image synthesizers [7, 23, 64] in that it disentangles the generative process into three stages separately for text-based anatomy placement, contrast-aware feature extraction and latent-guided image generation to address the multitude of labels, diversity of intensities and the incorporation of textual constraints in full-torso anatomy and CT volumes. We will elaborate on the specifics of our designs in the following sections.

3.1. Stage-I: Text-conditional Semantic Synthesizer

Current generative frameworks that use dedicated semantic synthesizers [10, 24] unintentionally introduce ambiguities as they struggle to capture the sharp transitions in labels near semantic boundaries due to an inaccurate data modeling. They also fail to provide an interface for more fine-grained and versatile control via free-form texts. Contrary to these methods, our Text-Conditional Semantics Synthesizer (TCSS) provides a text-based ambiguity-free solution by building upon a categorical diffusion model [28, 70] which directly assumes a discrete formulation. As shown

in Fig. 1(a), at its core, we train a categorical diffusion p_θ parameterized by θ that models the underlying distribution of mask volumes \mathbf{m} . At the first timestep, the diffusion variable $\mathbf{x}_0 = \mathbf{m} \in \{1, \dots, N\}^{H \times W \times D}$, where H , W , D separately denotes mask height, width and depth. In the forward process, \mathbf{x}_0 is gradually transformed to a categorical noise $\mathbf{x}_T \sim \mathcal{C}_N(\mathbf{x}_T; \mathbf{1}/N)$ in T timesteps under a noise schedule $\beta_{1:T}$, where \mathcal{C}_N denotes a categorical distribution of N categories (semantic classes). The forward probability transition can be described by

$$q(\mathbf{x}_t^i | \mathbf{x}_{t-1}^i) = \mathcal{C}_N(\mathbf{x}_t^i; (1 - \beta_t)\mathbf{e}(\mathbf{x}_{t-1}^i) + \beta_t \cdot \frac{\mathbf{1}}{N}) \in [0, 1]^N, \quad (1)$$

where the superscript i is the voxel index and $\mathbf{e}(\cdot)$ is a function that returns one-hot probability vectors from a categorical input. For compactness and ease of reading, from now on we will consider the diffusion process on an image with only one voxel to lose the superscript i , *i.e.* $H = W = D = 1$. Supposing voxels are independent, the formula derived below can be safely extended to images of any size. From the properties of Markov chains [28], the forward process of p_θ can be described as

$$q(\mathbf{x}_t | \mathbf{x}_0) = \mathcal{C}_N(\mathbf{x}_t; \bar{\alpha}_t \mathbf{e}(\mathbf{x}_0) + (1 - \bar{\alpha}_t) \cdot \frac{\mathbf{1}}{N}) \in [0, 1]^N, \quad (2)$$

where $\bar{\alpha}_t = \prod_{\tau=1}^t (1 - \beta_\tau)$.

To extract relevant information in the medical prompt for semantic placement, we use a text encoder \mathcal{E}_T pretrained on medical knowledge [62] to map the original prompt onto a latent space and perform cross-attention to guide anatomical generation by extracting spatial relation among anatomies. We interleave these cross-attention layers with a 3D U-Net [11] backbone to construct p_θ . Specifically, for each intermediate layer l in the 3D U-Net, the latent vector \mathbf{z}_l is first computed by

$$\mathcal{Q} = W^q(\mathbf{z}_{l-1}), \mathcal{K} = W^k(\mathcal{E}_T(\mathbf{p})), \mathcal{V} = W^v(\mathcal{E}_T(\mathbf{p})) \quad (3)$$

$$\mathbf{z}_l = \text{MLP}(\text{LayerNorm}(\text{Softmax}(\mathcal{Q}\mathcal{K}^\top / \sqrt{d})\mathcal{V})), \quad (4)$$

where W^q , W^k , and W^v are learnable projection mappings, \mathbf{p} is the input medical prompt and d is the context dimension. We train $p_\theta : [0, 1]^N \rightarrow [0, 1]^N$ by minimizing the Kullback-Leiber divergence between posterior and generator distributions across the diffusion process as in [27]. By denoting the posterior $q(\mathbf{x}_{t-1} | \mathbf{x}_t, \mathbf{x}_0) = \frac{q(\mathbf{x}_t | \mathbf{x}_{t-1})q(\mathbf{x}_{t-1} | \mathbf{x}_0)}{q(\mathbf{x}_t | \mathbf{x}_0)} \in [0, 1]^N$ as $\pi_t(\mathbf{x}_0)$, the overall training objective is

$$\mathcal{L} = \mathbb{E}_{t, \mathbf{x}_0} [\mathcal{D}_{KL}(\mathcal{C}_N(\mathbf{x}_{t-1}; \pi_t(\mathbf{x}_0)) || \mathcal{C}_N(\hat{\mathbf{x}}_{t-1}; p_\theta))], \quad (5)$$

with the hat notation distinguishing generated variables.

To avoid training instability, we make a similar reparameterization as in DDPM [27] for enhanced performance by

training a generator model on the same space as the input \mathbf{x}_0 . Instead of training a model $p_\theta(\mathbf{x}_t, \mathbf{p})$ that models on the distribution $\mathcal{C}_N(\hat{\mathbf{x}}_{t-1}; p_\theta)$, we will train and draw samples from its reparameterized version, denoted as $f_\theta = \mathcal{C}_N(\hat{\mathbf{x}}_0; f_\theta(\mathbf{x}_t, \mathbf{p}))$. The training loss \mathcal{L} needs to be modified accordingly: From the total probability formula, denoting $\mathbf{A} = (\pi_t(1), \dots, \pi_t(N))$, we have $p_\theta = \mathbf{A}f_\theta$. The voxel-wise loss for TCSS can be written as

$$\mathcal{L}_{TCSS} = \mathbb{E}_{t, \mathbf{x}_0} [\mathcal{D}_{KL}(\mathcal{C}_N(\mathbf{x}_{t-1}; \pi_t(\mathbf{x}_0)) || \mathcal{C}_N(\hat{\mathbf{x}}_{t-1}; \mathbf{A}f_\theta))]. \quad (6)$$

Under real settings where an image actually contains multiple voxels, the total loss \mathcal{L}_{TCSS} is averaged over each individual voxel.

At inference, TCSS samples from the distribution f_θ and computes the next denoising step by sampling on the generator distribution $S(\mathbf{A}f_\theta(\hat{\mathbf{x}}_t, \mathbf{p}))$, where S is the sampling scheme. Similar to [70], we sample by probability for timesteps $2 \sim T$ and take the index with max probability on the final denoising step to add stability to the generation process.

3.2. Stage-II: Contrast-aware Autoencoder

Similar to [9, 23], we use a pair of image autoencoder to extract high-level texture details from CT volumes while lowering memory demands to incorporate larger CT volumes. As shown in Fig. 1(b), similar to physicians examining different anatomical structures using different intensity windows, our Contrast-aware Autoencoder (CAE) strives to accurately accommodate the entire dynamic range of CT intensities with the help of a contrast-aware rescaler h . Formally,

$$h(\mathbf{x}) = k \max \left\{ \min \left\{ \frac{\mathbf{x} - w_c + w_r}{2w_r}, 1 \right\}, 0 \right\} + b, \quad (7)$$

where w_c and w_r are separately known as the window center and window radius. By definition, h truncates the intensity range of \mathbf{x} to $[w_c - w_r, w_c + w_r]$ and rescales them to $[b, k + b]$. At each training step, we randomly sample the window center w_c and window radius w_r from the intensity range of \mathbf{x} and use learnable k and b to map the truncated result back to the input space. Separately denoting the encoder and decoder halves of CAE as \mathcal{E}_I and \mathcal{D}_I , the l_1 reconstruction loss on an input volume \mathbf{v} can be defined as

$$\mathcal{L}_{rec} = \|h(\mathcal{D}_I(\mathcal{E}_I(\mathbf{v}))) - h(\mathbf{v})\|. \quad (8)$$

Aside from \mathcal{L}_{rec} , we follow the scheme of VQGAN [18] to introduce a quantization step \mathbf{q} with its adversarial components, learnable codebook \mathbf{c} and corresponding losses \mathcal{L}_{vq} to the autoencoder training process. Specifically, CAE encodes an input volume \mathbf{v} to its latent representation

$\mathcal{E}_I(\mathbf{v})$, replaces each feature \mathbf{z} with its nearest codebook entry $\mathbf{q}(\mathbf{z}) = \mathbf{c}_z$, and tries to recover the original volume \mathbf{v} from the quantized latent vectors. For adversarial losses, we use a frame discriminator \mathbf{D}_f that randomly chooses several planar slices from the CT volume and tries to distinguish between authentic slices and synthetic ones. Aside from this, we introduce a volume discriminator, \mathbf{D}_v , that does the same job from a volumetric viewpoint. These discriminators, separately focusing on anatomical details within a CT slice and the general structure of a CT volume, are not subject to contrast rescaling to avoid training instability and preserve the range of intensities for each organ. We also use perceptual loss based on a VGG-16 network [59, 72] \mathcal{L}_{perc} for reducing artifacts in image reconstruction as in [8]. Overall, the loss function for CAE is

$$\begin{aligned} \mathcal{L}_{CAE} = & \mathcal{L}_{rec}(h(\mathcal{D}_I(\mathcal{E}_I(\mathbf{v}))), h(\mathbf{v})) + \\ & \mathcal{L}_{vq}(\mathcal{E}_I(\mathbf{v}), \mathbf{c}) + \\ & \mathcal{L}_{perc}(h(\mathcal{D}_I(\mathcal{E}_I(\mathbf{v}))), h(\mathbf{v})) + \\ & \mathcal{L}_{disc}^{frame}(\mathcal{D}_I(\mathcal{E}_I(\mathbf{v}))[i], \mathbf{v}[i], \mathbf{D}_f) + \\ & \mathcal{L}_{disc}^{volume}(\mathcal{D}_I(\mathcal{E}_I(\mathbf{v})), \mathbf{v}, \mathbf{D}_v), \end{aligned} \quad (9)$$

where $\mathcal{L}_{vq}(\mathcal{E}_I(\mathbf{x}), \mathbf{c}) = \|\Omega(\mathcal{E}_I(\mathbf{x})) - \mathbf{c}_z\|_2^2 + \alpha \|\Omega(\mathbf{c}_z) - \mathcal{E}_I(\mathbf{x})\|_2^2$ and $\mathcal{L}_{disc}(\mathbf{x}', \mathbf{x}, \mathbf{D}) = \log \mathbf{D}(\mathbf{x}) + \log(1 - \mathbf{D}(\mathbf{x}'))$. Ω here is the stop-gradient operation.

3.3. Stage-III: Latent-guided Feature Generator

Since the encoded image and its semantic condition are not of the same shape, current practices usually downsample the mask volume for them to be consistent [8]. However, spatial relations between tumor and organs can be lost if the downsampling factor is too high. To promote preservation of semantic details and the textual guidance from medical prompts, we propose a Latent-guided Feature Generator (LFG) that operates entirely on the latent space to generate fine-grained image latents. As shown in Fig. 1(c), firstly, LFG encodes the torso semantics \mathbf{m}_A and tumor semantics \mathbf{m}_T divided from anatomies generated in Stage-I by several strided convolutional layers to downsample their spatial size. Between each downsampling convolution step, their semantic latents \mathbf{z}^A and \mathbf{z}^T are fused by attention layers

$$\mathbf{z}^A = \text{MLP}(\text{LayerNorm}(\text{Softmax}(\mathcal{Q}\mathcal{K}^\top / \sqrt{d})\mathcal{V})) \quad (10)$$

where $\mathcal{Q} = W^q(\mathbf{z}^A)$, $\mathcal{K} = W^k(\mathbf{z}^T)$, $\mathcal{V} = W^v(\mathbf{z}^T)$ are attention matrices and W^q , W^k , W^v are learnable mappings. Secondly, we use a diffusion model to approximate the distribution of image latents \mathbf{z}_0 . In the forward process, \mathbf{z}_0 is gradually converted to Gaussian noise $\mathbf{z}_T \sim \mathcal{N}(0, \mathbf{I})$ through T timesteps following a noise schedule $\beta'_{1:T}$

$$q(\mathbf{z}_t | \mathbf{z}_{t-1}) = \mathcal{N}(\mathbf{z}_t; \sqrt{1 - \beta'_t} \mathbf{z}_{t-1}, \beta'_t \mathbf{I}). \quad (11)$$

We follow a similar way as in Eq. 4 to use cross-attention layers to inject textual latents into our diffusion backbone and concatenate semantic latents \mathbf{z}^A , \mathbf{z}^T to the diffusion variable \mathbf{z}_t at each timestep. Finally, we construct the generative objective as in [27]:

$$\mathcal{L}_{LFG} = \mathbb{E}_{t, \epsilon \sim \mathcal{N}(0, \mathbf{I})} [\|\epsilon - f_\varphi(\mathbf{z}_t, \mathbf{z}^A, \mathbf{z}^T, \mathcal{E}_T(\mathbf{p}))\|_2^2], \quad (12)$$

where f_φ is the 3D U-Net [11] diffusion backbone parameterized by φ and $\mathcal{E}_T(\mathbf{p})$ is the textual latents encoded by the same text encoder described in Sec. 3.1. At inference time, f_φ gradually recovers an image latent $\hat{\mathbf{z}}_0$ by reverse sampling from random noise, which is then decoded into a valid CT image by the decoder \mathcal{D}_I from CAE.

4. Experiments

Dataset Construction (1) **Training:** We compile multiple CT datasets to train GuideGen, including 12 public imaging datasets with their corresponding clinical information from The Cancer Imaging Archive (TCIA) [12] and one real-world, private dataset (RJ) on colorectal cancer. Their groundtruth label maps are retrieved using pretrained multi-organ and tumor segmentation networks [34, 63]. This collected dataset is divided into 4534 training and 1179 validation cases used for generative training. (2) **Inference:** For downstream usability evaluation, we additionally incorporate BTCV [46] and AMOS22 [37] datasets for multi-organ segmentation tasks and MSD-Lung Tumors (LU), MSD-Colon Cancer (CO) [3], KiTS21 [26] (KI) datasets for tumor segmentation. The rest of the experiments are conducted on the validation split of TCIA and RJ. We will elaborate on our experimental settings in Appendix 6.1.

Evaluation Metrics The quality of our generated images are evaluated through the Learned Perceptual Image Patch Similarity (LPIPS), Fréchet Inception Distance (FID) and Fréchet Video Inception Distance (FVD) as per the general paradigm [23, 69]. We also use some these metrics to evaluate the quality of our masks due to a lack of dedicated metrics. Additionally, we report the Dice Similarity Coefficient (DSC) to evaluate image-mask consistency and the accuracy of several dedicated classifiers to measure alignment between image and certain feature described in the input prompt. Downstream Usability is evaluated through DSC and 95% Hausdorff Distance (HD_{95}) as commonly used in segmentation tasks [14, 38]. We set HD_{95} to 1000 to avoid NaN values for valid comparison when there are no semantic predictions. We calculate the standard deviation for usability metrics and use a double sided t -test to determine the statistical significance of GuideGen’s improvement over its nearest competitor and report them in Appendix 6.2.

Methods	infer.	model	comput.cost	Full Anatomy		Tumor Only	
	time(s)	param.(M)	(GFLOPs)	LPIPS	FID	LPIPS	FID
MedGen3D [24]	67.2	48.8	1295.7	0.70	201	0.29	33.5
LDM [57]	19.9	115.2	314.9	<u>0.67</u>	<u>98.6</u>	<u>0.30</u>	69.1
Hu’s [29]	0.8	-	0.15	-	-	0.32	64.8
GuideGen	54.1	49.1	2842.3	0.39	11.0	0.35	32.1

Table 1. Comparison studies of different semantic generation methods of full-torso anatomies and tumor-only binary masks.

Implementation Details All generative trainings are performed under an initial learning rate of 1×10^{-4} with a batch size of 1 per GPU on a multi-GPU(4) server and a patch size of $128 \times 128 \times 128$. The training processes use AdamW [49] optimizers with a momentum of 0.99, a weight decay of 1×10^{-5} and a linear learning rate scheduler to gradually decrease the learning rate to 0 over 500 epochs. For each diffusion model in TCSS and LFG, we use cosine noise schedule with 1000 timesteps and LFG uses DDIM denoising [60] of 200 timesteps to recover CT latents from Gaussian noise at a guidance scale of 2.5. Moreover, our CAE downsamples the original image by $4 \times$ and uses a codebook of 8192 entries.. At inference time, we train several segmentation networks using the official implementation of nnU-Net [34]. GuideGen itself is implemented using PyTorch [53] and all experiments are performed on 4 NVIDIA 4090 GPUs.

4.1. Main Results

Generation quality (1) **Mask quality:** To validate that GuideGen’s discrete formulation is indeed superior to current methods based on continuous modeling, we choose MedGen3D [24], which is based on DDPM [27], and LatentDiffusion [57] as baseline methods and infuse them with textual information in the same way as ours. Their generation results are rounded to the nearest integer to represent semantic information. We also compare with the Hu’s deformation method described in [29] for tumor generation. The results are shown in Tab. 1. It is evident that GuideGen performs better to baselines by a large margin on anatomy generation. This is not surprising as the ambiguity problem mentioned in Sec. 3.1 significantly hinders the performance of MedGen3D and LDM when the number of semantic classes is large. This problem persists but is less prominent as the number of semantic classes drops, as shown by synthesizing only the tumor masks, where GuideGen maintains comparable performance to comparison methods. (2) **Image quality:** We compare GuideGen’s image generation quality with a series of generative methods from different organs, including Pinaya’s and Med-DDPM [16, 54] for brain MRI generation, GenerateCT [23] and MedSyn [64] for lung CT generation, Zhuang’s [74] for abdominal CT generation and the generic medical generative framework MONAI-GM [55]. All of them are trained

Methods	input condition		inference time(s)	model parameters(M)	computational cost(GFLOPs)	generative metrics		
	mask	text				LPIPS	FID	FVD ¹²⁸
Pinaya’s [54]	N	Y	70.2	196.1	441.0	0.465	92.0	2091
GenerateCT[23]	N	Y	102.0	288.7	2167.9	0.521	151.7	4634
MONAI-GM [55]	G	N	74.1	166.5	461.9	0.406	57.7	1890
Zhuang’s [74]	G	N	45.5	81.2	2752.2	<u>0.327</u>	<u>23.2</u>	<u>1094</u>
MedDDPM [16]	G	N	42.4	80.5	2748.8	0.354	35.6	1299
MedSyn [64]	G	Y	24.7	115.1	1832.6	0.463	27.9	2267
GuideGen	G	Y	26.1	196.8	491.4	0.242	20.5	785
MONAI-GM [55]	R	N	74.1	166.5	461.9	0.393	54.6	1791
Zhuang’s [74]	R	N	45.5	81.2	2752.2	<u>0.335</u>	<u>39.1</u>	<u>1366</u>
MedDDPM [16]	R	N	42.4	80.5	2748.8	0.342	45.8	1619
MedSyn [64]	R	Y	24.7	115.1	1832.6	0.396	50.1	1960
GuideGen	R	Y	26.1	196.8	491.4	0.237	20.7	714

Table 2. Comparison studies of different image generation frameworks. The “128” superscript on FVD metric indicates we specifically consider CT volumes of 128 slices. A mask condition of ‘G’ or ‘R’ separately denotes semantic guidance from GuideGen-generated masks and real masks.

Methods	DSC										
	Spl.	Kid.	Liver	Sto.	Pan.	Lung	S.B.	Duo.	Colon	Heart	Avg.
MONAI-GM	<u>0.73</u>	<u>0.72</u>	<u>0.80</u>	<u>0.60</u>	0.43	0.84	<u>0.49</u>	0.35	0.55	<u>0.40</u>	<u>0.59</u>
Zhuang’s	0.43	0.43	0.62	0.36	0.21	0.69	0.37	0.23	0.26	0.24	0.38
MedDDPM	0.35	0.36	0.39	0.54	0.29	0.34	0.47	0.43	0.67	0.22	0.41
MedSyn	0.52	0.51	0.51	0.40	0.07	0.59	0.12	0.01	0.54	0.22	0.35
GuideGen	0.73	0.73	0.81	0.60	<u>0.42</u>	<u>0.83</u>	0.57	<u>0.37</u>	<u>0.60</u>	0.41	0.61

Table 3. Image-mask alignment between generated CT and their full-torso anatomical guidance. We report the DSC scores on ten major thoracic and abdominal organs.

using the train split from TCIA and RJ datasets. At inference time, for methods that dictates a mask input, we compare their performances with GuideGen’s performance under both GuideGen-generated and real masks to ensure a fair comparison, as shown in Tab. 2. We observe that GuideGen consistently outperforms existing methods in image quality under all metrics. Particularly, we notice that methods based solely on text conditions usually perform worse than those on semantic masks. We speculate this is because the highly diverse CT textures and intensity ranges among organs are difficult to recover without voxel-wise guidance, which reflects the necessity of our TCSS. Moreover, we see little discrepancy between metrics computed from samples generated using GuideGen-generated masks and real-world masks, reflecting that our TCSS can provide comparable quality to real masks. We also evaluate the generation results qualitatively as shown in Fig. 2 by observing that existing methods do not adapt well to the high dynamic range of CT intensities, appearing either too bright or too dark in specific body regions. In contrast, GuideGen maintains a realistic CT intensity range across the full torso, thanks to our proposed CAE.

Methods	Accuracy				
	Age	Gender	Race	Tumor Loc.	Avg.
Pinaya’s	0.06	0.35	0.10	0.17	0.17
GenerateCT	0.07	0.21	0.44	0.03	0.19
MedSyn	<u>0.17</u>	<u>0.74</u>	<u>0.51</u>	<u>0.47</u>	<u>0.47</u>
GuideGen	0.46	0.88	0.57	0.94	0.71

Table 4. Image-text alignment between generated CT and textual guidance. We report the accuracy of four dedicated classifiers on demographics and clinical features derived from the given medical prompts.

Generation-condition alignment We will thoroughly evaluate GuideGen’s conditional alignment from three aspects while comparing with other baselines. (1) **Image-mask alignment:** Image-mask alignment can be quantitatively measured by comparing predicted results from pre-trained segmentation models [63] on generated images with the actual masks given, with a higher alignment being a higher segmentation accuracy. We report the DSC of 10 major organs between predicted masks and real semantic condition input in Tab. 3. It can be seen that GuideGen behaves desirably for semantic correspondence, achieving a 2% gain on DSC compared to its nearest competitor. (2) **Image-text alignment:** To quantitatively evaluate the alignment between generated images and text prompt conditions, similar to [20, 23], we use a series of pretrained classifiers on certain features (age, gender, race, tumor location) to judge whether the generated images faithfully exhibits features specified in medical prompts. As shown in Tab. 4, images generated by our framework faithfully reflect the gender information and tumor location while outperforming other text-conditioned frameworks in preserving age-related and racial features. (3) **Mask-prompt alignment:** We measure mask-prompt alignment only qualitatively since little infor-

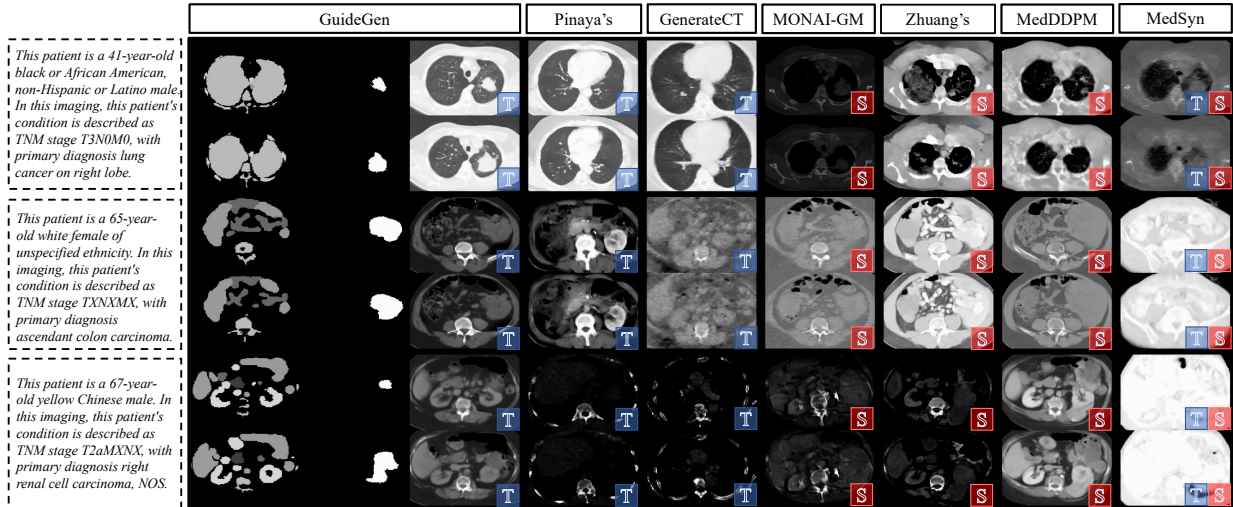


Figure 2. Qualitative results of different generation methods conditioned on the same textual prompts. Mask inputs to baseline models are generated with GuideGen. Two slices are shown per case. For better visualization, we use a CT intensity window of $[-975, -225]$ HU for displaying the chest region (rows 1-2), and $[-50, 150]$ HU for the abdominal region (rows 3-6) [58]. “T” and “S” stands for frameworks that requires textual inputs or semantic inputs, respectively. More qualitative results can be found in Appendix 6.2.

Dataset	Method	DSC													
		Spleen	Kidneys	Liver	Sto.	Pan.	Adr.	Eso.	Aorta	IVC	Gall.	Duo.	Blad.	PV&SV	Avg.
BTCV	Real	0.92	0.79	0.94	0.86	0.7	0.6	0.71	0.89	0.81	0.52	-	-	0.52	0.74
	MONAI-GM	<u>0.91</u>	0.89	0.94	0.80	0.61	0.44	0.60	0.84	0.78	0.29	-	-	0.48	0.69
	Zhuang's	0.90	0.88	0.95	0.83	0.65	0.54	0.69	<u>0.88</u>	0.82	<u>0.49</u>	-	-	<u>0.56</u>	0.74
	MedDDPM	0.92	0.90	0.95	<u>0.87</u>	<u>0.66</u>	0.54	0.68	0.88	0.84	0.39	-	-	0.49	<u>0.74</u>
	MedSyn	0.89	<u>0.90</u>	<u>0.96</u>	0.81	0.65	<u>0.56</u>	<u>0.70</u>	0.86	<u>0.86</u>	0.39	-	-	0.32	0.72
	GuideGen	0.94	0.92	0.96	0.91	0.74	0.59	0.73	0.91	0.87	0.49	-	-	0.65	0.79
AMOS	Real	0.95	0.94	0.96	0.89	0.81	0.67	0.78	0.92	0.87	0.72	0.76	0.82	-	0.84
	MONAI-GM	0.83	0.84	0.91	<u>0.74</u>	0.60	0.50	0.60	0.81	0.71	0.34	0.53	0.43	-	0.65
	Zhuang's	0.85	0.87	0.90	0.66	0.63	0.46	0.61	0.82	0.73	0.26	<u>0.55</u>	0.62	-	0.66
	MedDDPM	<u>0.86</u>	0.89	0.90	0.74	0.61	0.46	0.61	<u>0.86</u>	<u>0.76</u>	<u>0.43</u>	0.55	0.60	-	<u>0.69</u>
	MedSyn	0.85	<u>0.90</u>	<u>0.91</u>	0.70	<u>0.64</u>	<u>0.52</u>	<u>0.62</u>	0.80	0.69	0.21	0.53	<u>0.64</u>	-	0.67
	GuideGen	0.93	0.92	0.95	0.86	0.75	0.55	0.73	0.88	0.81	0.65	0.67	0.73	-	0.79

Table 5. Segmentation performance on multi-organ segmentation tasks using real or synthetic multi-organ masks from each generative framework.

mation except spatial relationships is depicted in generated masks. We give visualizations of mask-prompt alignment using mask synthesizers in MedGen3D (adapted by adding textual constraints to generation backbone as in Eq. 4) and GuideGen in Fig. 3 by varying tumor locations in our text prompt. It can be seen that our discrete formulation not only generates masks of accurate shape and structure, but also better preserves the spatial relationships between tumor and organs.

Usability in segmentation dataset synthesis To assess the usability in synthesizing datasets for segmentation purposes, we use nnU-Net [34] to train segmentation models using samples generated by different frameworks as well as real-world samples from established downstream datasets.

Sample synthesis is based on the anatomical masks and/or textual prompts in the validation split of our TCIA and RJ datasets. (1) **Multi-organ segmentation**: As shown in Tab. 5, segmentation models trained on samples generated from GuideGen can achieve comparable performance as those trained on real samples while outperforming those trained using synthetic samples generated with baseline frameworks, highlighting the generation quality of our generalized framework. (2) **Tumor segmentation**: Results for tumor segmentation (Tab. 6) show that our model can generate samples of lung tumors competitive with real ones while being more beneficial for other tumor segmentation tasks than baseline methods. Qualitative results can be found in Appendix 6.2.

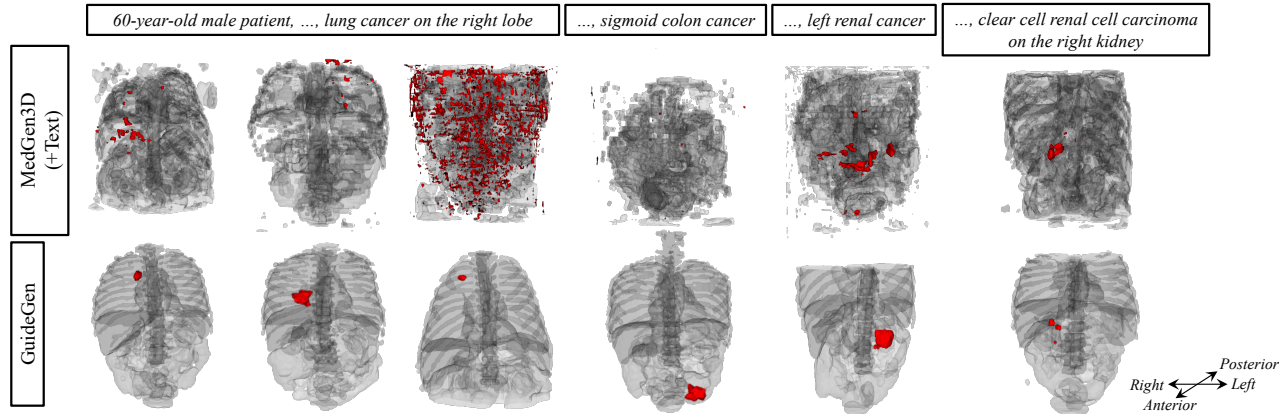


Figure 3. Qualitative results of generated full-torso anatomical masks, with tumor masks masked in red. For each textual constraint specified, GuideGen can provide faithful anatomies while being visibly superior thanks to our discrete formulation.

Method	DSC				HD ₉₅			
	LU	CO	KI	Avg.	LU	CO	KI	Avg.
Real	0.69	0.47	0.72	0.63	11.9	212.7	70.9	98.5
MONAI-GM	0.48	0.10	0.24	0.27	31.7	284.9	293.5	203.4
Zhuang’s	0.12	0.07	0.13	0.11	716.0	274.1	511.5	500.5
MedDDPM	0.10	0.09	0.29	0.16	776.0	273.6	119.4	389.7
MedSyn	0.44	0.11	0.39	0.31	33.1	267.4	309.0	203.2
GuideGen	0.69	0.24	0.51	0.48	10.5	244.0	154.5	136.3

Table 6. Segmentation performance on tumor segmentation tasks of different organs using real or synthetic cases from each method.

Mask Synthesizers	LPIPS	FID	FVD ¹²⁸
None	0.56	279	5981
LDM	0.40	61.4	2217
MedGen3D	0.41	69.6	2045
TCSS	0.24	20.5	785

Table 7. CT generation quality with different mask synthesizers. “None” denotes that the mask condition is removed (only the text condition is used).

GuideGen Settings		generative metrics			usability metrics	
CAE	LFG	LPIPS	FID	FVD ¹²⁸	Avg. DSC	Avg. HD ₉₅
N	N	0.35	48.1	1729	0.29	201.9
N	Y	0.36	46.4	1476	0.30	215.1
Y	N	0.25	23.1	1004	0.37	180.4
Y	Y	0.24	20.5	785	0.48	136.3

Table 8. Ablation studies on CAE and LFG modules. We use “Y”/“N” in CAE to indicate whether a contrast-aware rescaler is in effect and “Y”/“N” in LFG to indicate whether we use cross-attention in semantic guidance described in Sec. 3.3 as opposed to direct mask downsampling as in [8].

4.2. Ablation studies

We evaluate the effectiveness of each component in GuideGen, including the semantic synthesizer in TCSS, contrast-aware module in CAE and the efficacy of LFG as opposed to using latent diffusion models with straightforward mask downsampling. The usability metrics are computed in the same way as Tab. 6. From Tab. 7, we observe that CT synthesized using TCSS-generated semantics performs the best, and a lack of semantic guidance degrades performance drastically. Comparing Tab. 7 with Tab. 1, we can see an interesting trend that generated image quality is roughly in line with the quality of generated masks. Tab. 8 shows a clear boost in generative metrics by integrating contrast-awareness to image autoencoders for full-torso CT generation. The LFG strategy also provides for the image quality, and more importantly it benefits in preserving tumor semantics, as shown by the increase in usability metrics. Similarly, CAE also boosts performance in the downstream usability, we suspect this comes as a collateral benefit brought by an increased quality of CT synthesis.

5. Conclusion

In this paper, we have demonstrated a novel framework for generating paired 3D anatomies and 3D CT images covering the entire torso, conditioned on a free-text medical prompt. Firstly, we introduce a text-conditional semantic synthesizer with categorical modeling to aid in the text-based synthesis of semantic masks. Secondly, we propose a contrast-aware autoencoder to accommodate the high dynamic range of CT images. Finally, we propose a latent-guided feature generator to promote detail preservation and textual alignment over conventional resampling methods. Our model outperforms a range of existing methods under comprehensive evaluation, including generative quality, alignment with textual and semantic guidance, and usability

in training semantic segmentation models. Overall, our approach not only advances the state of the art in text-guided 3D CT generation but also lays a foundation for more robust training dataset synthesis for medical image analysis, making it highly impactful for clinical applications.

References

- [1] Oguz Akin, Pierre Elnajjar, Matthew Heller, Rose Jarosz, Bradley J Erickson, Shanah Kirk, Yueh Lee, Marston W Linehan, Rabindra Gautam, Raghu Vikram, Kimberly M Garcia, Charles Roche, Ermelinda Bonaccio, and Joe Filipini. The cancer genome atlas kidney renal clear cell carcinoma collection (TCGA-KIRC), 2016. [1](#)
- [2] Brad Albertina, Mark Watson, Chandra Holback, Rose Jarosz, Shanah Kirk, Yueh Lee, Kimberly Rieger-Christ, and John Lemmerman. The cancer genome atlas lung adenocarcinoma collection (TCGA-LUAD), 2016. [1](#)
- [3] Michela Antonelli, Annika Reinke, Spyridon Bakas, Keyvan Farahani, Annette Kopp-Schneider, Bennett A Landman, Geert Litjens, Bjoern Menze, Olaf Ronneberger, Ronald M Summers, et al. The medical segmentation decathlon. *Nature communications*, 13(1):4128, 2022. [5](#), [1](#), [2](#)
- [4] Yogesh Balaji, Seungjun Nah, Xun Huang, A Vahdat, J Song, K Kreis, and MY Liu. Ediffi: Text-to-image diffusion models with an ensemble of expert denoisers. arXiv 2022. *arXiv preprint arXiv:2211.01324*, 2022. [1](#)
- [5] Cancer Moonshot Biobank. Cancer moonshot biobank - colorectal cancer collection (CMB-CRC), 2022. [1](#)
- [6] Cancer Moonshot Biobank. Cancer moonshot biobank - lung cancer collection (CMB-LCA), 2022. [1](#)
- [7] Pierre Chambon, Christian Bluethgen, Jean-Benoit Delbrouck, Rogier Van der Sluijs, Małgorzata Połacin, Juan Manuel Zambrano Chaves, Tanishq Mathew Abraham, Shivanshu Purohit, Curtis P Langlotz, and Akshay Chaudhari. Roentgen: vision-language foundation model for chest x-ray generation. *arXiv preprint arXiv:2211.12737*, 2022. [1](#), [3](#)
- [8] Qi Chen, Xiaoxi Chen, Haorui Song, Zhiwei Xiong, Alan Yuille, Chen Wei, and Zongwei Zhou. Towards generalizable tumor synthesis. In *Proceedings of the IEEE/CVF Conference on Computer Vision and Pattern Recognition*, pages 11147–11158, 2024. [2](#), [4](#), [8](#)
- [9] Joseph Cho, Cyril Zakka, Dharampreet Kaur, Rohan Shad, Ross Wightman, Akshay Chaudhari, and William Hiesinger. Medisyn: Text-guided diffusion models for broad medical 2d and 3d image synthesis. *arXiv preprint arXiv:2405.09806*, 2024. [1](#), [4](#)
- [10] Yuetan Chu, Changchun Yang, Gongning Luo, Zhaowen Qiu, and Xin Gao. Anatomic-constrained medical image synthesis via physiological density sampling. In *International Conference on Medical Image Computing and Computer-Assisted Intervention*, pages 69–79. Springer, 2024. [3](#)
- [11] Özgün Çiçek, Ahmed Abdulkadir, Soeren S Lienkamp, Thomas Brox, and Olaf Ronneberger. 3d u-net: learning dense volumetric segmentation from sparse annotation. In *Medical Image Computing and Computer-Assisted Intervention–MICCAI 2016: 19th International Conference, Athens, Greece, October 17–21, 2016, Proceedings, Part II 19*, pages 424–432. Springer, 2016. [3](#), [5](#)
- [12] Kenneth Clark, Bruce Vendt, Kirk Smith, John Freymann, Justin Kirby, Paul Koppel, Stephen Moore, Stanley Phillips, David Maffitt, Michael Pringle, et al. The cancer imaging archive (tcia): maintaining and operating a public information repository. *Journal of digital imaging*, 26:1045–1057, 2013. [5](#), [1](#)
- [13] Emanuele Colleoni, Ricardo Sanchez Matilla, Imanol Luenengo, and Danail Stoyanov. Guided image generation for improved surgical image segmentation. *Medical Image Analysis*, page 103263, 2024. [3](#)
- [14] Linrui Dai, Wenhui Lei, and Xiaofan Zhang. Efficient subclass segmentation in medical images. In *International Conference on Medical Image Computing and Computer-Assisted Intervention*, pages 266–275. Springer, 2023. [1](#), [5](#)
- [15] Erick Costa de Farias, Christian Di Noia, Changhee Han, Evis Sala, Mauro Castelli, and Leonardo Rundo. Impact of gan-based lesion-focused medical image super-resolution on the robustness of radiomic features. *Scientific reports*, 11(1): 21361, 2021. [2](#)
- [16] Zolnamar Dorjsembe, Hsing-Kuo Pao, Sodtavilan Odonchimed, and Furen Xiao. Conditional diffusion models for semantic 3d brain mri synthesis. *IEEE Journal of Biomedical and Health Informatics*, 28(7):4084–4093, 2024. [5](#), [6](#)
- [17] Yilun Du and Igor Mordatch. Implicit generation and modeling with energy based models. *Advances in Neural Information Processing Systems*, 32, 2019. [2](#)
- [18] Patrick Esser, Robin Rombach, and Björn Ommer. Taming transformers for high-resolution image synthesis, 2020. [4](#)
- [19] Haoyang Fang, Boran Han, Shuai Zhang, Su Zhou, Cuixiong Hu, and Wen-Ming Ye. Data augmentation for object detection via controllable diffusion models. In *Proceedings of the IEEE/CVF Winter Conference on Applications of Computer Vision*, pages 1257–1266, 2024. [3](#)
- [20] Yu Gu, Jianwei Yang, Naoto Usuyama, Chunyuan Li, Sheng Zhang, Matthew P Lungren, Jianfeng Gao, and Hoifung Poon. Biomedjourney: Counterfactual biomedical image generation by instruction-learning from multimodal patient journeys. *arXiv preprint arXiv:2310.10765*, 2023. [6](#)
- [21] Qiushan Guo, Chuofan Ma, Yi Jiang, Zehuan Yuan, Yizhou Yu, and Ping Luo. Egc: Image generation and classification via a diffusion energy-based model. In *Proceedings of the IEEE/CVF International Conference on Computer Vision*, pages 9155–9164, 2023. [2](#)
- [22] Mustafa Hajji, Ghada Zamzmi, Rahul Paul, and Lokenda Thukar. Normalizing flow for synthetic medical images generation. In *2022 IEEE Healthcare Innovations and Point of Care Technologies (HI-POCT)*, pages 46–49. IEEE, 2022. [2](#)
- [23] Ibrahim Ethem Hamamci, Sezgin Er, Anjany Sekuboyina, Enis Simsar, Alperen Tezcan, Ayse Gulnihani Simsek, Sevval Nil Esirgun, Furkan Almas, Irem Doğan, Muhammed Furkan Dasdelen, et al. Generatect: text-conditional generation of 3d chest ct volumes. In *European Conference on Computer Vision*, pages 126–143. Springer, 2025. [1](#), [3](#), [4](#), [5](#), [6](#)

- [24] Kun Han, Yifeng Xiong, Chenyu You, Pooya Khosravi, Shanlin Sun, Xiangyi Yan, James S Duncan, and Xiaohui Xie. Medgen3d: A deep generative framework for paired 3d image and mask generation. In *International Conference on Medical Image Computing and Computer-Assisted Intervention*, pages 759–769. Springer, 2023. 1, 2, 3, 5
- [25] Anees Ur Rehman Hashmi, Ibrahim Almakky, Mohammad Areeb Qazi, Santosh Sanjeev, Vijay Ram Pappineni, Dwarikanath Mahapatra, and Mohammad Yaqub. Xreal: Realistic anatomy and pathology-aware x-ray generation via controllable diffusion model. *arXiv preprint arXiv:2403.09240*, 2024. 1, 3
- [26] Nicholas Heller, Fabian Isensee, Dasha Trofimova, Resha Tejpaul, Zhongchen Zhao, Huai Chen, Lisheng Wang, Alex Golts, Daniel Khapun, Daniel Shats, Yoel Shoshan, Flora Gilboa-Solomon, Yasmeen George, Xi Yang, Jianpeng Zhang, Jing Zhang, Yong Xia, Mengran Wu, Zhiyang Liu, Ed Walczak, Sean McSweeney, Ranveer Vasdev, Chris Hornung, Rafat Solaiman, Jamee Schoepfoerster, Bailey Abernathy, David Wu, Safa Abdulkadir, Ben Byun, Justice Spriggs, Griffin Struyk, Alexandra Austin, Ben Simpson, Michael Hagstrom, Sierra Virnig, John French, Nitin Venkatesh, Sarah Chan, Keenan Moore, Anna Jacobsen, Susan Austin, Mark Austin, Subodh Regmi, Nikolaos Papanikolopoulos, and Christopher Weight. The kits21 challenge: Automatic segmentation of kidneys, renal tumors, and renal cysts in corticomedullary-phase ct, 2023. 5, 1, 2
- [27] Jonathan Ho, Ajay Jain, and Pieter Abbeel. Denoising diffusion probabilistic models. *Advances in neural information processing systems*, 33:6840–6851, 2020. 3, 5
- [28] Emiel Hoogeboom, Didrik Nielsen, Priyank Jaini, Patrick Forré, and Max Welling. Argmax flows and multinomial diffusion: Learning categorical distributions. *Advances in Neural Information Processing Systems*, 34:12454–12465, 2021. 3
- [29] Qixin Hu, Yixiong Chen, Junfei Xiao, Shuwen Sun, Jieneng Chen, Alan L Yuille, and Zongwei Zhou. Label-free liver tumor segmentation. In *Proceedings of the IEEE/CVF Conference on Computer Vision and Pattern Recognition*, pages 7422–7432, 2023. 1, 3, 5
- [30] Peng Huang, Xue Gao, Lihong Huang, Jing Jiao, Xiaokang Li, Yuanyuan Wang, and Yi Guo. Chest-diffusion: A light-weight text-to-image model for report-to-cxr generation. In *2024 IEEE International Symposium on Biomedical Imaging (ISBI)*, pages 1–5. IEEE, 2024. 1
- [31] Yongzhi Huang, Jinxin Zhu, Haseeb Hassan, Liyilei Su, and Jingyu Li. Label-efficient multi-organ segmentation method with diffusion model. *arXiv preprint arXiv:2402.15216*, 2024. 1
- [32] Alex Ling Yu Hung, Kai Zhao, Haoxin Zheng, Ran Yan, Steven S Raman, Demetri Terzopoulos, and Kyunghyun Sung. Med-cdiff: Conditional medical image generation with diffusion models. *Bioengineering*, 10(11):1258, 2023. 2
- [33] José Antonio Iglesias, José María Monterrubio, María Paz Sesmero, and Araceli Sanchis. Generation and evaluation of medical images based on diffusion models. In *2024 IEEE International Conference on Evolving and Adaptive Intelligent Systems (EAIS)*, pages 1–8. IEEE, 2024. 2
- [34] Fabian Isensee, Paul F Jaeger, Simon AA Kohl, Jens Petersen, and Klaus H Maier-Hein. nnu-net: a self-configuring method for deep learning-based biomedical image segmentation. *Nature methods*, 18(2):203–211, 2021. 5, 7, 1
- [35] Khawar Islam, Muhammad Zaigham Zaheer, Arif Mahmood, and Karthik Nandakumar. Diffusemix: Label-preserving data augmentation with diffusion models. In *Proceedings of the IEEE/CVF Conference on Computer Vision and Pattern Recognition*, pages 27621–27630, 2024. 3
- [36] Pranav Jeevan, Neeraj Nixon, and Amit Sethi. Normalizing flow based metric for image generation. *arXiv preprint arXiv:2410.02004*, 2024. 2
- [37] Yuanfeng Ji, Haotian Bai, Chongjian Ge, Jie Yang, Ye Zhu, Ruimao Zhang, Zhen Li, Lingyan Zhanng, Wanling Ma, Xiang Wan, et al. Amos: A large-scale abdominal multi-organ benchmark for versatile medical image segmentation. *Advances in neural information processing systems*, 35:36722–36732, 2022. 5, 1, 2
- [38] Yankai Jiang, Zhongzhen Huang, Rongzhao Zhang, Xiaofan Zhang, and Shaoting Zhang. Zept: Zero-shot pan-tumor segmentation via query-disentangling and self-prompting. In *Proceedings of the IEEE/CVF Conference on Computer Vision and Pattern Recognition*, pages 11386–11397, 2024. 5
- [39] Amirhossein Kazerouni, Ehsan Khodapanah Aghdam, Moein Heidari, Reza Azad, Mohsen Fayyaz, Ilker Hacıhaliloglu, and Dorit Merhof. Diffusion models in medical imaging: A comprehensive survey. *Medical Image Analysis*, 88:102846, 2023. 3
- [40] Kyuri Kim, Yoonho Na, Sung-Joon Ye, Jimin Lee, Sung Soo Ahn, Ji Eun Park, and Hwiyoung Kim. Controllable text-to-image synthesis for multi-modality mr images. In *Proceedings of the IEEE/CVF Winter Conference on Applications of Computer Vision*, pages 7936–7945, 2024. 1, 3
- [41] Diederik P Kingma and Max Welling. Auto-encoding variational bayes, 2022. 2
- [42] Shanahv Kirk, Yueh Lee, Prasanna Kumar, Joe Filippini, Brad Albertina, Mark Watson, Kimberly Rieger-Christ, and John Lemmerman. The cancer genome atlas lung squamous cell carcinoma collection (TCGA-LUSC), 2016. 1
- [43] Shanah Kirk, Yueh Lee, Cheryl A Sadow, and Seth Levine. The cancer genome atlas rectum adenocarcinoma collection (TCGA-READ), 2016. 1
- [44] Shanah Kirk, Yueh Lee, Cheryl A Sadow, Seth Levine, Charles Roche, Ermelinda Bonaccio, and Joe Filiippini. The cancer genome atlas colon adenocarcinoma collection (TCGA-COAD), 2016. 1
- [45] Nicholas Konz, Yuwen Chen, Haoyu Dong, and Maciej A Mazurowski. Anatomically-controllable medical image generation with segmentation-guided diffusion models. *arXiv preprint arXiv:2402.05210*, 2024. 3
- [46] Bennett Landman, Zhoubing Xu, J Igelsias, Martin Styner, Thomas Langerak, and Arno Klein. Miccai multi-atlas labeling beyond the cranial vault—workshop and challenge. In *Proc. MICCAI Multi-Atlas Labeling Beyond Cranial Vault—Workshop Challenge*, page 12, 2015. 5, 1, 2

- [47] Marston Linehan, Rabindra Gautam, Shanah Kirk, Yueh Lee, Charles Roche, Ermelinda Bonaccio, Joe Filippini, Kimberly Rieger-Christ, John Lemmerman, and Rose Jarosz. The cancer genome atlas cervical kidney renal papillary cell carcinoma collection (TCGA-KIRP), 2016. 1
- [48] Marston W Linehan, Rabindra Gautam, Cheryl A Sadow, and Seth Levine. The cancer genome atlas kidney chromophobe collection (TCGA-KICH), 2016. 1
- [49] Ilya Loshchilov and Frank Hutter. Decoupled weight decay regularization. *arXiv preprint arXiv:1711.05101*, 2017. 5
- [50] National Cancer Institute Clinical Proteomic Tumor Analysis Consortium (CPTAC). The clinical proteomic tumor analysis consortium clear cell renal cell carcinoma collection (CPTAC-CCRCC), 2018. 1
- [51] National Cancer Institute Clinical Proteomic Tumor Analysis Consortium (CPTAC). The clinical proteomic tumor analysis consortium lung adenocarcinoma collection (CPTAC-LUAD), 2018. 1
- [52] National Cancer Institute Clinical Proteomic Tumor Analysis Consortium (CPTAC). The clinical proteomic tumor analysis consortium lung squamous cell carcinoma collection (CPTAC-LSCC), 2018. 1
- [53] Adam Paszke, Sam Gross, Francisco Massa, Adam Lerer, James Bradbury, Gregory Chanan, Trevor Killeen, Zeming Lin, Natalia Gimelshein, Luca Antiga, et al. Pytorch: An imperative style, high-performance deep learning library. *Advances in neural information processing systems*, 32, 2019. 5
- [54] Walter HL Pinaya, Petru-Daniel Tudosiu, Jessica Dafflon, Pedro F Da Costa, Virginia Fernandez, Parashkev Nachev, Sebastien Ourselin, and M Jorge Cardoso. Brain imaging generation with latent diffusion models. In *MICCAI Workshop on Deep Generative Models*, pages 117–126. Springer, 2022. 1, 5, 6
- [55] Walter HL Pinaya, Mark S Graham, Eric Kerfoot, Petru-Daniel Tudosiu, Jessica Dafflon, Virginia Fernandez, Pedro Sanchez, Julia Wolleb, Pedro F Da Costa, Ashay Patel, et al. Generative ai for medical imaging: extending the monai framework. *arXiv preprint arXiv:2307.15208*, 2023. 5, 6
- [56] Ryan Po, Wang Yifan, Vladislav Golyanik, Kfir Aberman, Jonathan T Barron, Amit Bermano, Eric Chan, Tali Dekel, Aleksander Holynski, Angjoo Kanazawa, et al. State of the art on diffusion models for visual computing. In *Computer Graphics Forum*, page e15063. Wiley Online Library, 2024. 3
- [57] Robin Rombach, Andreas Blattmann, Dominik Lorenz, Patrick Esser, and Björn Ommer. High-resolution image synthesis with latent diffusion models, 2021. 5
- [58] E. Seeram. *Computed Tomography: Physical Principles, Clinical Applications, and Quality Control*. Elsevier, 2015. 7, 3
- [59] Karen Simonyan and Andrew Zisserman. Very deep convolutional networks for large-scale image recognition. *arXiv preprint arXiv:1409.1556*, 2014. 4
- [60] Jiaming Song, Chenlin Meng, and Stefano Ermon. Denoising diffusion implicit models. *arXiv preprint arXiv:2010.02502*, 2020. 5
- [61] Li Sun, Junxiang Chen, Yanwu Xu, Mingming Gong, Ke Yu, and Kayhan Batmanghelich. Hierarchical amortized gan for 3d high resolution medical image synthesis. *IEEE journal of biomedical and health informatics*, 26(8):3966–3975, 2022. 2
- [62] Yu Sun, Shuohuan Wang, Shikun Feng, Siyu Ding, Chao Pang, Junyuan Shang, Jiayang Liu, Xuyi Chen, Yanbin Zhao, Yuxiang Lu, et al. Ernie 3.0: Large-scale knowledge enhanced pre-training for language understanding and generation. *arXiv preprint arXiv:2107.02137*, 2021. 3
- [63] Jakob Wasserthal, Hanns-Christian Breit, Manfred T Meyer, Maurice Pradella, Daniel Hinck, Alexander W Sauter, Tobias Heye, Daniel T Boll, Joshy Cyriac, Shan Yang, et al. Totalsegmentator: Robust segmentation of 104 anatomic structures in ct images. *Radiology: Artificial Intelligence*, 5(5), 2023. 5, 6, 1
- [64] Yanwu Xu, Li Sun, Wei Peng, Shuyue Jia, Katelyn Morrison, Adam Perer, Afroz Zandifar, Shyam Visweswaran, Motahhare Eslami, and Kayhan Batmanghelich. Medsyn: Text-guided anatomy-aware synthesis of high-fidelity 3d ct images. *IEEE Transactions on Medical Imaging*, 2024. 1, 3, 5, 6
- [65] Ling Yang, Zhilong Zhang, Yang Song, Shenda Hong, Runsheng Xu, Yue Zhao, Wentao Zhang, Bin Cui, and Ming-Hsuan Yang. Diffusion models: A comprehensive survey of methods and applications. *ACM Computing Surveys*, 56(4): 1–39, 2023. 1
- [66] Qingsong Yao, Li Xiao, Peihang Liu, and S Kevin Zhou. Label-free segmentation of covid-19 lesions in lung ct. *IEEE transactions on medical imaging*, 40(10):2808–2819, 2021. 1
- [67] Jee Seok Yoon, Chenghao Zhang, Heung-II Suk, Jia Guo, and Xiaoxiao Li. Sadm: Sequence-aware diffusion model for longitudinal medical image generation. In *International Conference on Information Processing in Medical Imaging*, pages 388–400. Springer, 2023. 2
- [68] Yongrui Yu, Hanyu Chen, Zitian Zhang, Qiong Xiao, Wenhui Lei, Linrui Dai, Yu Fu, Hui Tan, Guan Wang, Peng Gao, et al. Ct synthesis with conditional diffusion models for abdominal lymph node segmentation. *arXiv preprint arXiv:2403.17770*, 2024. 1, 2
- [69] Yongrui Yu, Yannian Gu, Shaoting Zhang, and Xiaofan Zhang. Meddiff-fm: A diffusion-based foundation model for versatile medical image applications. *arXiv preprint arXiv:2410.15432*, 2024. 5
- [70] Lukas Zbinden, Lars Doorenbos, Theodoros Pissas, Adrian Thomas Huber, Raphael Sznitman, and Pablo Márquez-Neila. Stochastic segmentation with conditional categorical diffusion models. In *Proceedings of the IEEE/CVF International Conference on Computer Vision*, pages 1119–1129, 2023. 3, 4
- [71] Chenlu Zhan, Yu Lin, Gaoang Wang, Hongwei Wang, and Jian Wu. Medm2g: Unifying medical multi-modal generation via cross-guided diffusion with visual invariant. In *Proceedings of the IEEE/CVF Conference on Computer Vision and Pattern Recognition*, pages 11502–11512, 2024. 1
- [72] Richard Zhang, Phillip Isola, Alexei A Efros, Eli Shechtman,

and Oliver Wang. The unreasonable effectiveness of deep features as a perceptual metric. In *CVPR*, 2018. [4](#)

[73] Tao Zhou, Qi Li, Huiling Lu, Qianru Cheng, and Xiangxiang Zhang. Gan review: Models and medical image fusion applications. *Information Fusion*, 91:134–148, 2023. [2](#)

[74] Yan Zhuang, Benjamin Hou, Tejas Sudharshan Mathai, Pritam Mukherjee, Boah Kim, and Ronald M Summers. Semantic image synthesis for abdominal ct. In *International Conference on Medical Image Computing and Computer-Assisted Intervention*, pages 214–224. Springer, 2023. [5](#), [6](#)

GuideGen: A Text-Guided Framework for Full-torso Anatomy and CT Volume Generation

Supplementary Material

6. Appendix

Code Disclosure Statement All source code, include model training, data processing, downstream evaluation and metric computation are contained in the `code.zip` submitted along with this appendix, and they will be publicly released should our paper be accepted.

6.1. Datasets and Implementation Details

6.1.1. Dataset Details

Training datasets We compiled 12 TCIA [12] datasets on three common types of cancer (lung, kidney and colon). To supplement the scarcity of publicly available colon cancer multimodal (paired CT and clinical information) dataset, we also include one private real-world dataset, dubbed RJ, for colorectal cancer. The preprocessing of all the collected unstandardized samples include the following four steps: (a) **Data cleansing**: All of the collected CT samples are reoriented into RAS orientation and resampled to isotopic spacing, with duplicate, impaired, partial DICOM series identified and removed. (b) **Label Extraction**: CT images in the collected dataset are segmented by TotalSegmentator [63] and pretrained models [34] on their respective tumor types to retrieve both multi-organ and tumor segmentation masks; their corresponding clinical information are retrieved using a private medical GPT in a certain format: *The patient is {demographics group}*. *In this imaging, the patient’s condition is described as {clinical information}*. (c) **Noise Removal**: Organ labels belonging to the same anatomical class (e.g. individual rib label and the anatomical class ribs) are merged into one semantic label to mitigate noise in the multi-organ labels. Samples with no or erroneous (tumor predictions outside organ prediction) tumor mask predictions are discarded. (d) **Dataset Preparation**: We randomly split the processed images into 4534 training cases and 1179 validation cases. Specifically, we use the CT, clinical information and masks in the training split to train GuideGen as well as baseline models, detailed description of each training dataset of choice are listed in Tab. 9, and we showcase the distribution of each demographics group in TCIA and RJ datasets in Fig. 4.

Dataset Name	Description	No. Patients	No. Cases	No. Cases after pp.
CMB-CRC [5]	Colorectal Cancer	54	237	50
TCGA-READ [43]	Rectum Cancer	3	34	4
TCGA-COAD [44]	Colon Cancer	25	93	21
RJ	Colorectal Cancer	4005	4418	3235
CPTAC-CCRCC [50]	Renal Cancer	262	727	248
TCGA-KICH [48]	Renal Cancer	15	109	26
TCGA-KIRC [1]	Renal Cancer	267	2654	734
TCGA-KIRP [47]	Renal Cancer	33	376	56
CPTAC-LSCC [52]	Pulmonary Cancer	212	238	236
CPTAC-LUAD [51]	Pulmonary Cancer	244	242	71
CMB-LCA [6]	Pulmonary Cancer	97	696	64
TCGA-LUAD [2]	Pulmonary Cancer	69	624	120
TCGA-LUSC [42]	Pulmonary Cancer	37	279	92

Table 9. **Datasets used for generative training, quality evaluation and alignment measurement.** “RJ” is our private dataset on colorectal cancer while “No. Cases after pp.” is short for “The number of cases after preprocessing”.

Inference datasets We we choose the abdominal split of Multi-Atlas Labeling Beyond the Cranial Vault (BTCV) [46] and Abdominal [37] Multi-Organ Segmentation (AMOS) datasets and evaluate the segmentation performance on some of their organ labels that overlap with our interest. Additionally, for tumor segmentation, we select two Medical Segmentation Decathlon (MSD) [3] datasets along with the Kidney Tumor Segmentation (KiTS) [26] dataset, separately for pulmonary,

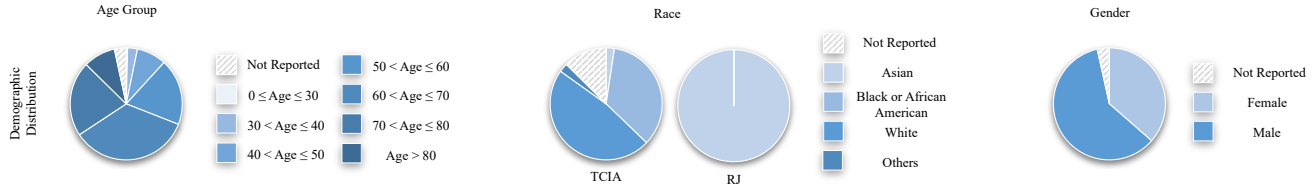


Figure 4. **Demographics distribution for TCIA and RJ datasets** used for generative training as well as quality and alignment evaluations.

Dataset Name	Description	No. Train cases	No. Inference cases	Semantic Classes Reported
BTCV [46]	Abdominal Organs	24	6	Spl., Kid., Liver, Sto., Pan., Adr., Eso., Aorta, IVC, Gall., PV&SV
AMOS [37]	Abdominal Organs	240	60	Spl., Kid., Liver, Sto., Pan., Adr., Eso., Aorta, IVC, Gall., Duo., Blad.
MSD-Lung [3]	Pulmonary Cancer	40	10	Lung Tumor
MSD-Colon [3]	Colon Cancer	80	20	Colon Tumor
KiTS [26]	Renal Cancer	210	90	Kidney Tumor

Table 10. **Datasets used for downstream segmentation evaluation.** Abbreviations: Spl.: Spleen, Kid.: Kidneys, Sto.: Stomach, Pan.: Pancreas, Adr.: Adrenal Glands, Eso.: Esophagus, IVC: Inferior Vena Cava, Gall.: Gallbladder, PV&SV: Portal Vein and Splenic Vein, Duo.: Duodenum, Blad.: Urinary Bladder.

colorectal and renal cancer. Their details are documented in Tab. 10. We also downsamples the training cases in each inference dataset to $128 \times 128 \times 128$ to ensure a fair comparison with the $128 \times 128 \times 128$ volumes generated by GuideGen.

6.1.2. Implementation Details

GuideGen In Stage-I, we use TCSS to generate 19 major pleural, abdominal and pelvic structure* and 1 tumor semantics. The reason for not choosing more organ labels lies largely in that other anatomies suffer from relatively poor multi-organ segmentation accuracies. It should be noted that our framework should simulate as many anatomies as possible if the quality of training data is ensured. The model channels in each layer of our backbone U-Net network are 32, 64, 128, 256, respectively, with $8\times$ downsampling at the U-Net bottleneck. Each layer consists of two ResNet convolution blocks and we add a cross-attention layer to the first and third layer to integrate textual information.

In Stage-II, our CAE downsamples the CT image by $4\times$ and operates on a codebook of 8192 entries, each with a feature dimension of 8. The frame discriminator \mathbf{D}_f in CAE chooses 8 slices for discriminative loss computation in each iteration. We also set a min-max normalization for CT images prior to their input into CAE model: CT images are linearly rescaled in such a way that the CT intensities of the range $[-1500, 1500]$ HU resides in the interval $[-1, 1]$ after rescaling. In this way, we can recover CT intensities from the decoder half of CAE after LFG generation by multiplying the result by the multiplier 1500.

In Stage-III, we first encode tumor and organ semantics separately to a vector with a feature dimension of 4 and spatial dimension $4\times$ smaller than original input (which computes to $32 \times 32 \times 32$ in our experiment setting). As we jointly generate tumor and organ semantics in the first stage, we follow the following steps to retrieve label for them individually: Firstly, for 19 organ labels $l_A = \{l_A^1, \dots, l_A^{19}\}$, 1 tumor label l_T and 1 background label l_B , the final step of TCSS sampling trajectory will output a probability vector $\hat{\mathbf{x}}_0 \in [0, 1]^{21 \times H \times W \times D}$. H , W and D are spatial dimensions, which all equals 128 in our setting. Secondly, we perform argmax operation on the channel dimension to retrieve these semantic masks, specifically, the organ semantics \mathbf{m}_A and tumor semantics \mathbf{m}_T are retrieved by

$$\mathbf{m}_A = \underset{l_A, l_B}{\text{argmax}} \hat{\mathbf{x}}_0; \mathbf{m}_T = \underset{l_A, l_T, l_B}{\delta(\text{argmax} \hat{\mathbf{x}}_0, l_T)}. \quad (13)$$

That is, we discard the probabilities of tumor label when retrieving organ semantics, and $\delta(x, y)$ here is the impulse function that takes 1 on the entry i when $x[i]$ equals y and 0 otherwise. The encoded semantic latents, along with the image feature encoded by the encoder half of CAE are then concatenated to a latent vector with a feature dimension of 16, which is fed into

*The 19 major anatomical structure of choice are: Lung, Heart, Ribs, Vertebra, Esophagus, Aorta, Inferior Vena Cava, Liver, Spleen, Stomach, Duodenum, Gallbladder, Splenic Vein and Portal Vein, Kidneys, Adrenal Glands, Pancreas, Small Bowel, Colon (with rectum) and Urinary Bladder, covering major anatomies throughout the torso.

a backbone U-Net with the same structure as that described in TCSS. Loss is computed between the U-Net output and the image latent.

Baseline models We follow official implementation available online for each baseline method, and adjust their model parameters (mainly the channel numbers for each convolutional layer) so that they can generate $128 \times 128 \times 128$ volumes under our physical setting (NVIDIA RTX 4090 GPUs). We also skip the final super-resolution module in some baselines [23, 64] since it has no relevance to conditional generation and can be added to any generative framework as a postprocessing module.

6.2. Supplementary Results

This section provides tables and figures that serves as a supplement to the main results displayed in the main article.

6.2.1. Qualitative Results

In this subsection, we first showcase GuideGen’s generative performance of both unhealthy and healthy samples using randomly chosen demographic and clinical descriptions from TCIA and RJ datasets in Fig. 5. Secondly, we display multi-organ segmentation results and tumor segmentation results separately in Fig. 6 and Fig. 7. For slices located in the pleural region, we display them using a normalization window at $[-975, -225]$ HU, while for slices in the abdominal and pelvic regions, we display them using a normalization window at $[-50, 150]$ HU as recommended in [58].

6.2.2. Quantitative Results

We display standard variances of each metric used in multi-organ segmentation and tumor segmentation evaluations separately in Tab. 11 and Tab. 12 in this subsection. We also report the validation accuracy and AUROC of demographic or clinical classifiers used to assess image-prompt alignment in Tab. 13. They are implemented based on the encoder half of U-Net 3D networks [11] and trained on the training split of TCIA and RJ datasets. Classifier classes are chosen following the demographic classes in Fig. 4 and tumor locations in Tab. 9. Metrics in Tab. 13 are computed on the validation split of TCIA and RJ datasets.

6.2.3. Utilizing GuideGen for Dataset Synthesis or Augmentation

Finally, in Tab. 14, we tested the usability of generated samples by using different number of GuideGen-generated cases for dataset synthesis (segmentation models trained with no real cases required) or dataset augmentation (using GuideGen-generated cases as a complement to the real cases to train segmentation models). We randomize the demographic features and clinical severity in GuideGen’s input while fixing the tumor location to a certain organ. It can be seen that on the multi-organ segmentation tasks, using 1000 synthetic cases as augmentation achieves an average performance gain of 6% across BTCV and AMOS datasets, while segmentation models trained using synthetic data alone achieves comparable performance to those trained with real data. For tumor segmentation tasks, performance gains are also observed using synthetic data as augmentation at a large scale, achieving a surplus in DSC of 9%, 1% and 5% separately for three different tumor types at 1000 synthetic cases. Using synthetic data for dataset synthesis also provides a solid starting point, especially for lung tumors, as seen in the last 6 rows of Tab. 14.

Dataset	Method	Std. DSC													
		Spl.	Kid.	Liver	Sto.	Pan.	Adr.	Eso.	Aorta	IVC	Gall.	Duo.	Blad.	PV&SV	Avg.
BTCV	Real	0.295	0.332	0.132	0.224	0.271	0.191	0.180	0.318	0.365	0.326	-	-	0.208	0.258
	MONAI-GM	0.013	0.018	0.011	0.090	0.098	0.070	0.124	0.073	0.077	0.310	-	-	0.116	0.091
	Zhuang's	0.024	0.017	0.010	0.046	0.089	0.049	0.093	0.027	0.041	0.394	-	-	0.156	0.086
	MedDDPM	0.014	0.014	0.010	0.049	0.107	0.072	0.102	0.061	0.044	0.352	-	-	0.141	0.088
	MedSyn	0.015	0.012	0.007	0.027	0.113	0.086	0.111	0.062	0.031	0.398	-	-	0.173	0.094
	GuideGen	0.007	0.007	0.006	0.022	0.054	0.075	0.091	0.013	0.030	0.381	-	-	0.062	0.068
AMOS	Real	0.065	0.068	0.044	0.172	0.198	0.172	0.168	0.133	0.163	0.292	0.172	0.256	-	0.146
	MONAI-GM	0.170	0.157	0.166	0.176	0.209	0.187	0.166	0.166	0.170	0.292	0.187	0.270	-	0.176
	Zhuang's	0.127	0.100	0.082	0.190	0.224	0.213	0.192	0.156	0.175	0.332	0.213	0.228	-	0.167
	MedDDPM	0.062	0.043	0.062	0.199	0.192	0.204	0.186	0.090	0.123	0.304	0.204	0.231	-	0.141
	MedSyn	0.070	0.045	0.087	0.103	0.172	0.149	0.163	0.085	0.131	0.281	0.149	0.252	-	0.127
	GuideGen	0.025	0.041	0.017	0.132	0.147	0.152	0.141	0.084	0.088	0.271	0.152	0.240	-	0.112

Table 11. **Segmentation variance on multi-organ segmentation tasks using real or synthetic cases from each method.** The significance of our improvement over the second-best framework is tested using a two-sided t -test, with a p -value of 0.016 and 0.001 respectively for two datasets. Abbreviations: Spl.: Spleen, Kid.: Kidneys, Sto.: Stomach, Pan.: Pancreas, Adr.: Adrenal Glands, Eso.: Esophagus, IVC: Inferior Vena Cava, Gall.: Gallbladder, Duo.: Duodenum, Blad.: Urinary Bladder, PV&SV: Portal Vein and Splenic Vein. Some of the semantic classes reported are not consistent with the original dataset since they are merged as described in 6.1.2.

Method	Std. DSC				Std. HD ₉₅			
	LU	CO	KI	Avg.	LU	CO	KI	Avg.
Real	0.22	0.38	0.32	0.31	20.9	394.7	242.0	219.2
MONAI-GM	0.23	0.14	0.33	0.23	29.6	403.1	497.1	309.9
Zhuang's	0.12	0.19	0.27	0.19	28.8	408.5	483.6	307.0
MedDDPM	0.21	0.19	0.38	0.26	21.2	409.0	275.9	235.4
MedSyn	0.35	0.18	0.29	0.27	45.5	411.4	426.0	294.3
GuideGen	0.21	0.10	0.40	0.24	20.7	357.2	465.7	281.2

Table 12. **Segmentation variance on tumor segmentation tasks of different organs using real or synthetic cases from each method.** The significance of our improvement over the second-best framework is tested using a two-sided t -test, with a p -value of 0.002, 0.01 and 0.06 respectively for three datasets. When there are no tumor predictions, HD₉₅ is set to be 1000 to avoid ∞ values for a valid comparison. Abbreviations: LU: pulmonary cancer, CO: colorectal cancer, KI: renal cancer.

Classifier Type	Metrics		Classifier Classes
	Accuracy	AUROC	
Age Group	0.74	0.69	[0,30], (30,40], (40,50], (50,60], (60,70], (70,80], (80, ∞)
Race	0.76	0.64	Asian, Black or African American, White, Others
Gender	0.92	0.87	Female, Male
Tumor Location	0.89	0.73	Lung, Kidney, Colon and rectum

Table 13. **Classifier performance on the validation split of TCIA and RJ datasets.** Image-prompt alignment is assessed by evaluating the accuracy between features specified in input prompts and those predicted from generated images using these classifiers.

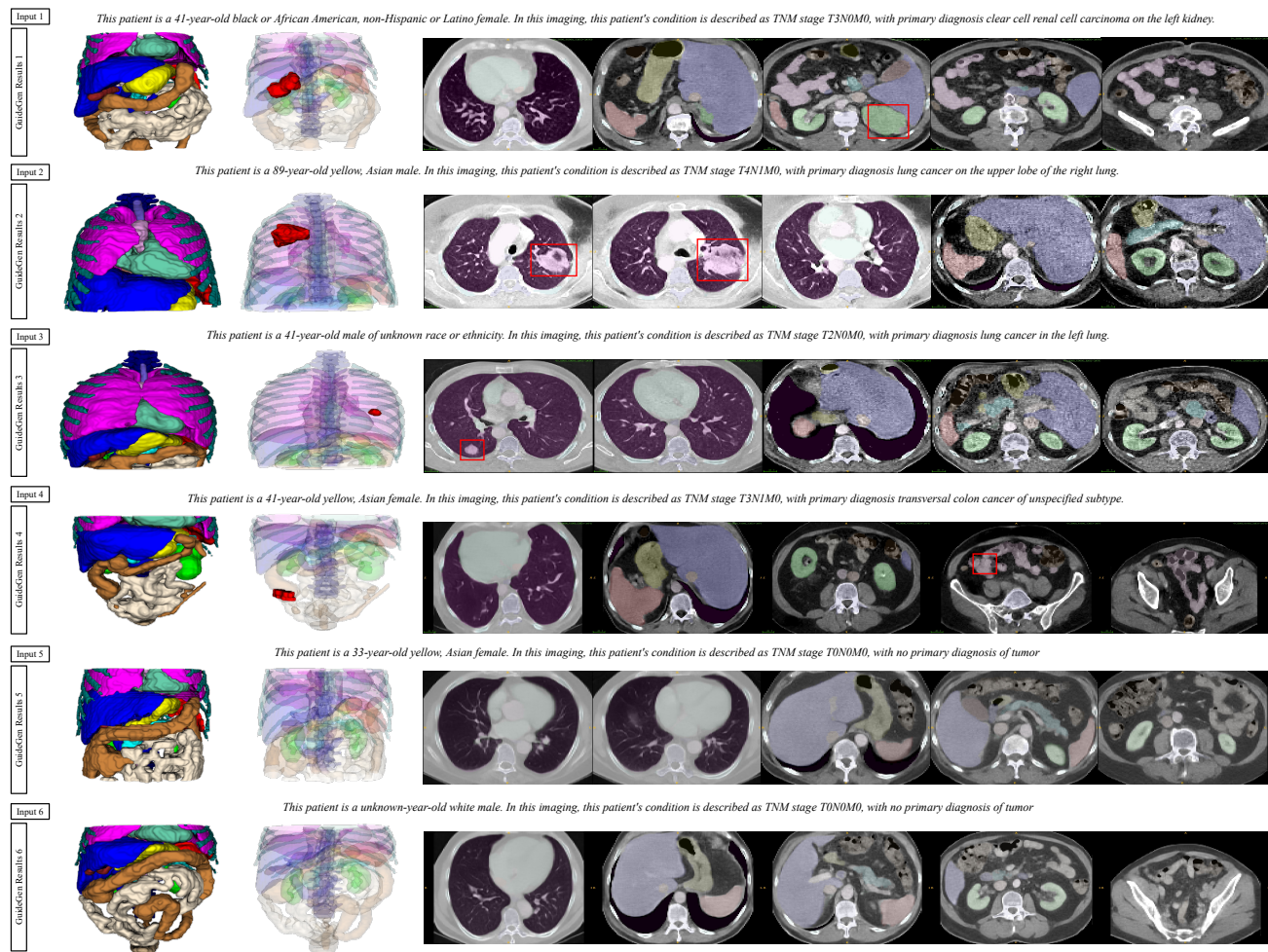


Figure 5. **Samples generated by GuideGen for qualitative assessment.** Five slices are shown in each case along with the multi-organ anatomies and tumor semantics (if any). We mark the bounding box of tumor labels in the CT slices shown using red outlines. Note that the first four cases accommodate a tumor site for the clinical description in the medical prompt while the last two has no tumor indication from the input prompt and generate a healthy anatomy and CT instead.

Dataset	No. Real cases for training	No. Synthetic cases for training / Avg. DSC				
		0	100	200	500	1000
BTCV	0	0.00	0.69	0.79	0.79	0.81
	24	0.74	0.81	0.82	0.83	0.83
AMOS	0	0.00	0.64	0.79	0.81	0.81
	240	0.84	0.82	0.85	0.87	0.87
MSD-Lung	0	0.00	0.64	0.69	0.71	0.73
	40	0.69	0.72	0.75	0.77	0.78
MSD-Colon	0	0.00	0.07	0.24	0.27	0.33
	80	0.47	0.41	0.49	0.50	0.48
KiTS	0	0.00	0.46	0.51	0.59	0.63
	210	0.72	0.72	0.72	0.74	0.77

Table 14. **Performance gain by using different numbers of GuideGen’s generated samples for segmentation dataset synthesis or augmentation.** We report the average DSCs for segmentation performance on each dataset. For reference, the main article reports the performance of segmentation models trained using all real training cases as opposed to those trained using 200 synthetic cases for each dataset.

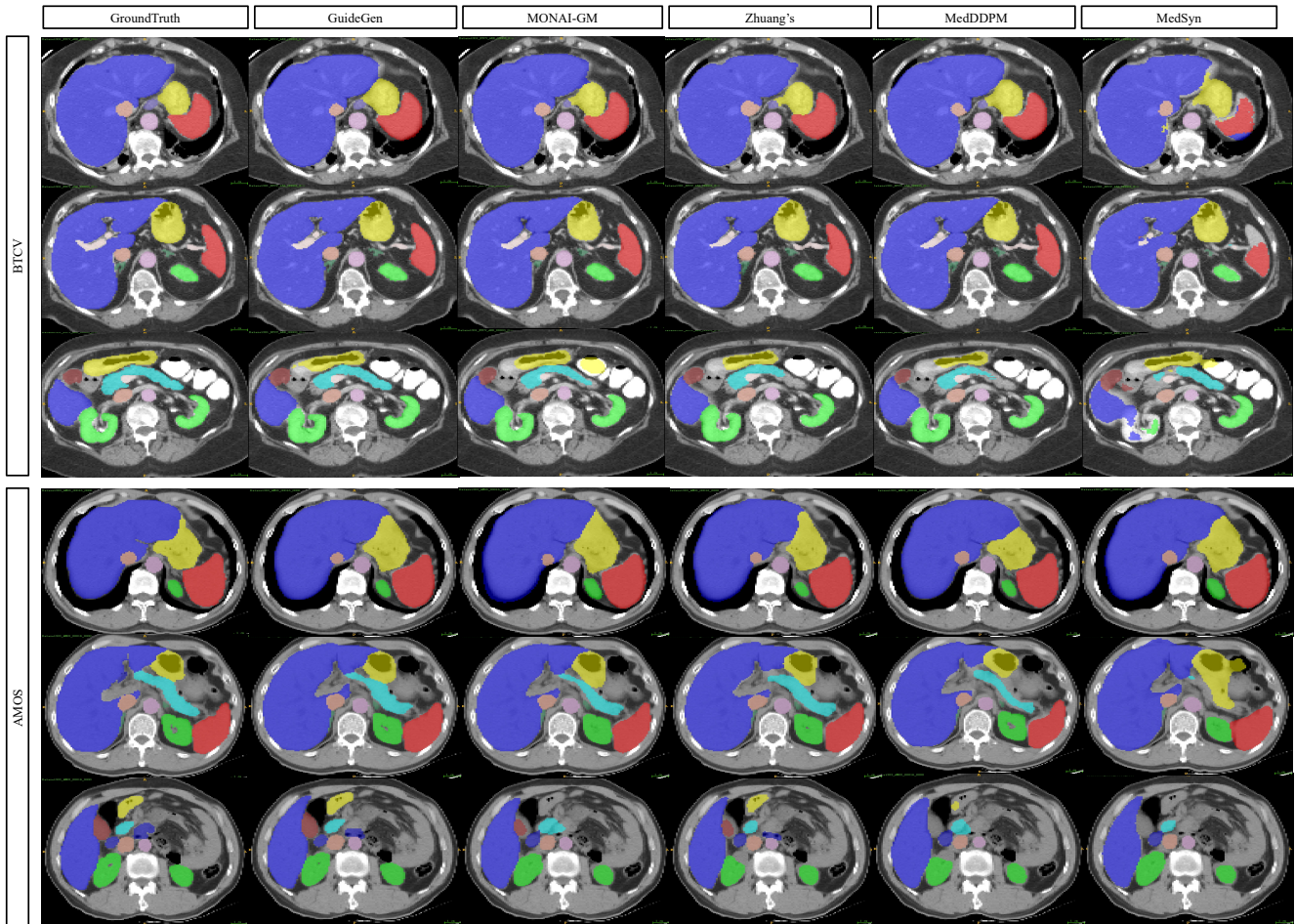


Figure 6. **Qualitative results for multi-organ segmentations on BTCV and AMOS datasets.** Three slices are shown in each case displayed.

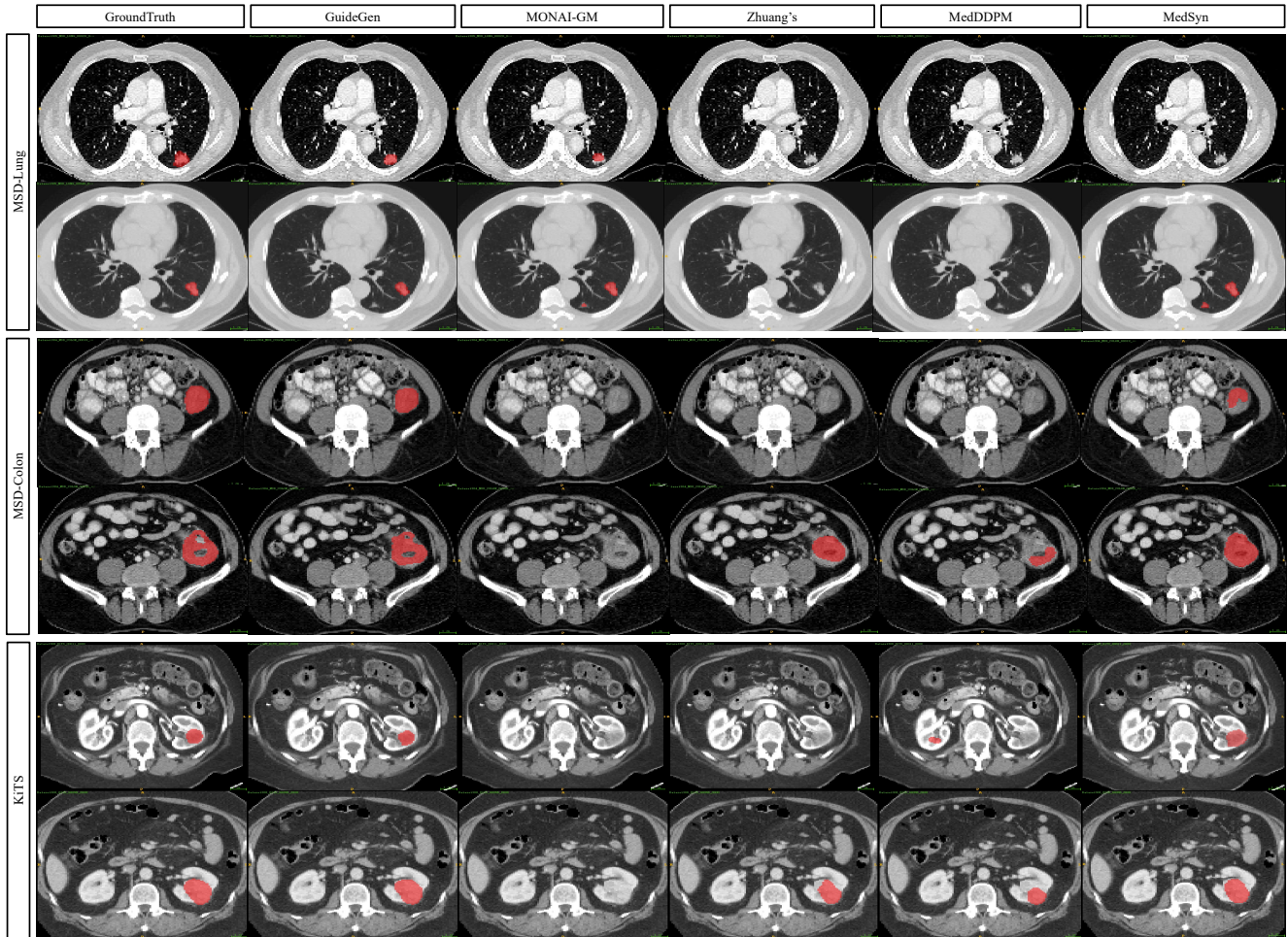


Figure 7. Qualitative results for tumor segmentations on MSD-Lung, MSD-Colon and KiTS datasets. One slice is chosen for each case, which is centered at the largest transversal section of the tumor.